

HEAT TRANSFER COMPARISON INVESTIGATION OF THE PERMANENT MAGNET SYNCHRONOUS MOTOR FOR ELECTRIC VEHICLES BASED ON THE BOUNDARY ELEMENT METHOD AND THE FINITE ELEMENT METHOD

Jiacheng ZHANG^{1}, Haixu ZHANG², Zining LIU³*

^{*1} National Engineering Research Center of Large Electric Machines and Heat Transfer Technology (School of Electrical and Electronic Engineering, Harbin University of Science and Technology), Harbin, China

² Technology and Innovation Research Center, HIT Robot Group Co., Ltd, Taizhou, China

³ Dongfang Electronics Co.,Ltd, Yantai, China

* Corresponding author; E-mail: qingjide@foxmail.com

In the field of heat transfer in permanent magnet synchronous motors (PMSMs) for electric vehicles (EVs), the boundary element method (BEM) has been applied for the first time to calculate the steady-state temperature of the PMSM with a spiral water-cooled system. In this investigation, the boundary-integration equation (BIE) for the steady-state heat transfer problem of a water-cooled PMSM is first derived on the basis of thermodynamic theory, and the system of constant coefficient differential equations is obtained by discretizing its boundaries, while the temperature results obtained from the BEM are compared with the finite element method (FEM) results. Furthermore, the temperature distribution and heat transfer characteristics obtained from the FEM and BEM were verified twice using the PMSM prototype and test platform. The results show that the maximum relative error between the temperature calculation results of FEM and BEM is 1.97%, and the maximum relative error between the results of BEM and the test does not exceed 3%, which finally verifies the validity and accuracy of BEM in solving the heat transfer problems of water-cooled PMSMs.

Key words: Heat transfer research, Boundary element method, Finite element method, Permanent magnet synchronous motor, Numerical methods comparison

1. Introduction

In recent years, the rapid development of vehicle electrification has shown great advantages and long-term prospects in terms of greenhouse gas reduction and fossil fuel savings [1-3]. In this background, permanent magnet synchronous motors (PMSMs) play an indispensable role in the process of vehicle electrification due to their high torque, high power density and excellent NVH [4-5]. Compared to ordinary motors, PMSMs usually have to push the electromagnetic and thermal loads to their limits in order to meet the requirements of acceleration performance as well as range, which leads to significantly higher electromagnetic losses and heat generation per unit volume, higher magnetic circuit saturation and increased difficulty in heat transfer design [6-7]. Therefore, thermal management is currently still a limiting factor for PMSMs to achieve higher energy densities. Without

effective thermal management, high temperatures will accelerate the deterioration of insulation materials and eventually cause insulation breakage. Worse still, after the PMSMs approach or break the thermal limit, the permanent magnets will produce irreversible demagnetization, seriously affecting the safety and service life of the PMSMs [8-10]. Consequently, it is essential to investigate the heat transfer mechanism of PMSMs and to find numerical methods that can establish and truly reflect the internal heat transfer characteristics of motors, so as to provide a theoretical basis and data support for the subsequent upgrading and optimization of thermal design.

The finite element method (FEM) is a widely used numerical analysis method for heat transfer problems in PMSMs for electric vehicles (EVs) [11-13]. The FEM uses volumetric discretization to divide the calculation area into elements, which do not overlap with each other but are connected to each other. The solution of the entire calculation area is accomplished by generating a stable solution between the elements by means of an error function within each element. Li et al. proposed a finite element model for the study of 3-D fluid thermal coupling in order to avoid thermal demagnetization of the permanent magnets due to high temperatures. The finite element calculations of this model led to the determination of the fluid velocity and temperature distribution of different parts of the motor, which ultimately demonstrated the effectiveness of the hybrid cooled system [14]. To investigate the relationship between cooled system performance and torque density limits, Vansompel et al. integrated direct air-cooled and indirect water-cooled techniques, and determined the continuous stator current density under different thermal loads by 3-D thermal finite element simulations [15]. Boglietti et al. predicted the thermal behavior of the PMSM based on the FEM and searched for a model in which the heat transfer performance and magnetic performance were in balance in a large number of motor samples, ultimately providing a sample of temperature predictions and experimental data to support the calibration of the motor finite element model [16-17]. Although FEM is well developed and a reliable numerical analysis method in the field of heat transfer in PMSMs for EVs, FEM requires discretization of the entire model and calculation area, generates a large number of grids, takes a long time to calculate and requires high computer hardware. With the development of heat transfer, numerical computational methods have advanced tremendously and increasingly more numerical methods are being used to solve heat transfer problems. Among them, the Boundary element method (BEM) has greatly improved the computational efficiency by generating a number of elements on the boundary of the computational region and discretizing the boundaries of each element, which finally generates a smaller number of elements [18-19]. In addition to dealing with most of the heat transfer problems to which the FEM is adapted, the BEM can also deal with infinite domain problems that cannot be solved by the FEM. Qin et al. proposed a novel coupled BEM-FEM method to investigate 2-D steady-state heat transfer in multi-scale structures and clarified the differences between BEM and FEM in 2-D steady-state thermal analysis [20-21]. Si et al. used BEM to numerically investigate the performance of photovoltaic-thermal (PVT) collectors and finally determined the thermal and electrical efficiencies of the collectors when using different heat sinks [22]. Zhu et al. designed and simulated a new type of heat exchanger using nanofluid, and used BEM to calculate the heat transfer efficiency of the heat exchanger under different cooling conditions [23].

It is remarkable that the application of BEM to the heat transfer problem of PMSMs for EVs is rare. Based on this, this work combines the advantages of BEM and FEM to investigate the heat transfer problem of PMSMs. Firstly, a boundary-integration equation (BIE) is derived for the steady-state heat transfer problem of water-cooled PMSMs. Secondly, the system of constant coefficient

differential equations is obtained by boundary discretization of the BIE and the temperature results obtained from the BEM are compared with the simulation results of the FEM. Furthermore, the PMSM for EVs with a spiral water-cooled system was made, and the temperature distribution and heat transfer characteristics obtained from the FEM and BEM were verified twice. The results demonstrate that BEM has the advantages of low computational effort and high computational accuracy, and is a numerical calculation method that can effectively solve the heat transfer problem of PMSMs for EVs. Moreover, we believe that the results of the investigation can provide new ideas for improving the thermal management of PMSMs for EVs, and provide data support and application value for boundary element studies of PMSMs.

2. Numerical methods

2.1. Boundary element analysis

In the heat transfer analysis of the PMSM for EVs, water is used as the cooling fluid. The water-cooled system contains no internal heat source, the heat source comes from the motor. Therefore, in the PMSM 3-D steady state heat transfer problem, the BEM control equation can be expressed as follows:

$$k(\frac{\partial^2}{\partial x_1^2} + \frac{\partial^2}{\partial x_2^2} + \frac{\partial^2}{\partial x_3^2})u(x, t) = \rho c \dot{u}(x, t) \quad (1)$$

Where $u(x, t)$ is the temperature at point x at time t , k is the heat transfer coefficient, ρ is the material density, c is the specific heat capacity, t_0 is the initial moment.

The BEM boundary conditions are set as follows:

$$\begin{cases} u(x, t) = \bar{u}(x, t), \forall x \in S_u \\ q(x, t) = k \frac{\partial u(x, t)}{\partial \mathbf{n}(x)} = \bar{q}(x, t), \forall x \in S_q \end{cases} \quad (2)$$

Where q is the heat flux, \bar{q} is the known heat homogeneity on the boundary, S_u denotes a Dirichlet-type boundary, S_q denotes a Neumann-type boundary, $S_u + S_q = \Gamma$ is all the boundaries of the computational domain Ω , and \mathbf{n} is the normal direction vector outside the boundary.

The initial BEM conditions are set as follows:

$$\begin{cases} u(x, t_0) = u_0(x), \forall x \in \Omega \\ q(x, t_0) = q_0(x), \forall x \in \Gamma \end{cases} \quad (3)$$

For the control equations of the PMSM steady-state heat transfer problem, we apply the weighted residual approach to derive the boundary-integration equations of the control equations. After we introduce the weighting function, the weighted equation of equation (1) is:

$$\int_{\Omega} u^*(y, x) k \nabla^2 u(x, t) d\Omega(x) = \int_{\Omega} u^*(y, x) \rho c \dot{u}(x, t) d\Omega(x) \quad (4)$$

The domain integration on the left-hand side of equation (4) is transformed into the following integral equation according to Gauss' scattering theorem:

$$\begin{aligned} & \int_{\Omega} u^*(y, x) k \nabla^2 u(x, y) d\Omega(x) = \\ & \int_{\Gamma} u^*(y, x) q(x, t) d\Gamma(x) - \\ & \int_{\Gamma} u(x, t) k \frac{\partial u^*(y, x)}{\partial \mathbf{n}(x)} d\Gamma(x) - k u(y, t) \end{aligned} \quad (5)$$

After applying the boundary topology to the BEM mathematical model of the PMSM, the following BIE can be obtained:

$$\begin{aligned} & -\int_{\Omega} u^*(y, x) \rho c \dot{u}(x, t) d\Omega(x) = \\ & C(y) k u(y, t) + \int_{\Gamma} u(x, t) q^*(y, x) d\Gamma(x) - \\ & \int_{\Gamma} u^*(y, x) q(x, t) d\Gamma(x) \end{aligned} \quad (6)$$

We can clearly see the domain integration to the left of the equal sign in equation (6), which contains the unknown quantity $\dot{u}(x, t)$ in its kernel of integration, and the radial basis function (RBF) is used to interpolate the approximation of the unknown quantity, and the RBF chosen is as follows:

$$f_i(x) = \sqrt{r^2 + s^2} \quad (7)$$

Where r is the distance from the RBF interpolation point to the source point; s is the shape parameter; and i is the total number of interpolation points. After exact interpolation, the following BIE can be obtained, and at this point the BIE no longer involves the domain integration.

$$\begin{aligned} & C(y) u(y, t) + \frac{1}{k} \int_{\Gamma} u(x, t) q^*(y, x) d\Gamma(x) \\ & - \frac{1}{k} \int_{\Gamma} u^*(y, x) q(x, t) d\Gamma(x) = \\ & \frac{\rho c}{k} \sum_i \alpha_i \left[C_i(y) \hat{u}_i(y, x) + \int_{\Gamma} \hat{u}_i(y, x) q^*(y, x) d\Gamma(x) - \right. \\ & \left. \int_{\Gamma} u^*(y, x) \hat{q}_i(y, x) d\Gamma(x) \right] \end{aligned} \quad (8)$$

In the BIE (8), the first-order derivative term of temperature with respect to time has been replaced by an equivalent boundary integral, since the domain integration is no longer involved. Unlike the FEM, because the unknowns u and q are taken at the boundary, the BEM only needs to discretize the boundary, which gives:

$$\begin{aligned} & C(y) u(y, t) - \\ & \frac{1}{k} \sum_j \sum_m \int_{\Gamma_j} u^*(y, x) q(x_m, t) N_m(x) d\Gamma(x) + \\ & \frac{1}{k} \sum_j \sum_m \int_{\Gamma_j} u(x_m, t) q^*(y, x) N_m(x) d\Gamma(x) = \\ & \frac{\rho c}{k} \left[C(y) \sum_i \alpha_i(t) \hat{u}_i(y) + \right. \\ & \sum_i \sum_j \sum_m \int_{\Gamma_j} \hat{u}_i(x_m) q^*(y, x) N_m(x) d\Gamma(x) \alpha_i(t) - \\ & \left. \sum_i \sum_j \sum_m \int_{\Gamma_j} u^*(y, x) \hat{q}_i(x_m) N_m(x) d\Gamma(x) \alpha_i(t) \right] \end{aligned} \quad (9)$$

Where j is the number of boundary cells and m is the number of nodes in the cell, we use a boundary cell with 16 nodes, i.e. $m=16$. After distributing the source points to all the boundary nodes, we obtain the following matrix:

$$\overset{bb}{H} \overset{b}{u}(t) - \overset{bb}{G} \overset{b}{q}(t) = \rho c \left(\overset{bb}{H} \overset{bd}{U} - \overset{bb}{G} \overset{bd}{Q} \right) \overset{d}{\alpha}(t) \quad (10)$$

Where \mathbf{H} and \mathbf{G} are the influence coefficient matrices; the letters above the matrices are the matrix dimensions, where b is the number of boundary nodes and d is the number of nodes in the domain. We eventually rewrite the matrix in the following form:

$$\begin{bmatrix} {}^{bb} \mathbf{H} & -\mathbf{G} \end{bmatrix} \begin{bmatrix} {}^b \mathbf{u}(t) \\ {}^b \mathbf{q}(t) \end{bmatrix} = \rho c \begin{bmatrix} {}^{bb} \mathbf{H} & -\mathbf{G} \end{bmatrix} \begin{bmatrix} {}^{bd} \hat{\mathbf{U}} \\ {}^{bd} \hat{\mathbf{Q}} \end{bmatrix} \mathbf{F}^{-1} \dot{\mathbf{u}}^d(t) \quad (11)$$

Adding the boundary conditions to equation (11) yields:

$$\begin{bmatrix} {}^{bb} \mathbf{H} & -\mathbf{G} \\ {}^{bb} \mathbf{C}_1 & \mathbf{C}_2 \end{bmatrix} \begin{bmatrix} {}^b \mathbf{u}(t) \\ {}^b \mathbf{q}(t) \end{bmatrix} = \rho c \begin{bmatrix} {}^{bb} \mathbf{H} & -\mathbf{G} \\ 0 & 0 \end{bmatrix} \begin{bmatrix} {}^{bd} \hat{\mathbf{U}} \\ {}^{bd} \hat{\mathbf{Q}} \end{bmatrix} \mathbf{F}^{-1} \dot{\mathbf{u}}^d(t) + \begin{bmatrix} 0 \\ {}^b \mathbf{C}_3(t) \end{bmatrix} \quad (12)$$

Considering the spiral water-cooled system and its internal nodes, equation (11) can be rewritten in the following form:

$$\begin{bmatrix} {}^{db} \mathbf{H} & -\mathbf{G} \end{bmatrix} \begin{bmatrix} {}^b \mathbf{u}(t) \\ {}^b \mathbf{q}(t) \end{bmatrix} + \mathbf{u}^d(t) = \rho c \left(\begin{bmatrix} {}^{db} \mathbf{H} & -\mathbf{G} \end{bmatrix} \begin{bmatrix} {}^{bd} \hat{\mathbf{U}} \\ {}^{bd} \hat{\mathbf{Q}} \end{bmatrix} + \hat{\mathbf{U}}^{\ddot{d}} \right) \mathbf{F}^{-1} \dot{\mathbf{u}}^d(t) \quad (13)$$

At this stage, the values of the nodes in the PMSM calculation area can be expressed as:

$$\begin{aligned} \dot{\mathbf{u}}^d(t) &= \mathbf{A}^{\ddot{d}} \mathbf{u}^d(t) + \mathbf{p}^d(t) \\ \mathbf{A}^{\ddot{d}} &= -\mathbf{F}^{\ddot{d}} \left(\begin{bmatrix} {}^{db} \mathbf{H} & -\mathbf{G} \end{bmatrix} \mathbf{Z} - \left(\rho c \begin{bmatrix} {}^{db} \mathbf{H} & -\mathbf{G} \end{bmatrix} \begin{bmatrix} {}^{bd} \hat{\mathbf{U}} \\ {}^{bd} \hat{\mathbf{Q}} \end{bmatrix} + \hat{\mathbf{U}}^{\ddot{d}} \right) \right)^{-1} \\ \mathbf{p}^d(t) &= -\mathbf{F}^{\ddot{d}} \left(\begin{bmatrix} {}^{db} \mathbf{H} & -\mathbf{G} \end{bmatrix} \mathbf{Z} - \left(\rho c \begin{bmatrix} {}^{db} \mathbf{H} & -\mathbf{G} \end{bmatrix} \begin{bmatrix} {}^{bd} \hat{\mathbf{U}} \\ {}^{bd} \hat{\mathbf{Q}} \end{bmatrix} + \hat{\mathbf{U}}^{\ddot{d}} \right) \right)^{-1} \times \\ &\quad \begin{bmatrix} {}^{db} \mathbf{H} & -\mathbf{G} \end{bmatrix} {}^{2b} \mathbf{e}(t) \end{aligned} \quad (14)$$

The general solution of Eq. (14) is:

$$\mathbf{u}^d = e^{\mathbf{A}^{\ddot{d}}(t-t_0)} \mathbf{u}_0^d + \int_{t_0}^t e^{\mathbf{A}^{\ddot{d}}(t-\tau)} \mathbf{p}^d(\tau) d\tau \quad (15)$$

By using a level-by-level calculation to precisely identify the boundary nodes in the PMSM calculation area, the exponential function of the final matrix can be subdivided into the following forms:

$$\begin{aligned} e^{\mathbf{A}^{\ddot{d}}\tau} &= \mathbf{I} + \mathbf{A}^{\ddot{d}}(t-t_0) + \frac{1}{2!} \mathbf{A}^{\ddot{d}2}(t-t_0)^2 + \dots + \\ &\quad \frac{1}{n!} \mathbf{A}^{\ddot{d}n}(t-t_0)^n + \dots = \sum_n \frac{1}{n!} \mathbf{A}^{\ddot{d}n}(t-t_0)^n \end{aligned} \quad (16)$$

The Taylor series expansion on the left-hand side of the equal sign of equation (16) has been omitted in this paper due to the space limitation of the article. Furthermore, in order to more clearly illustrate our process of applying BEM and FEM for comparative heat transfer investigation of the PMSM, the calculation process of the two numerical methods is shown in Fig. 1.

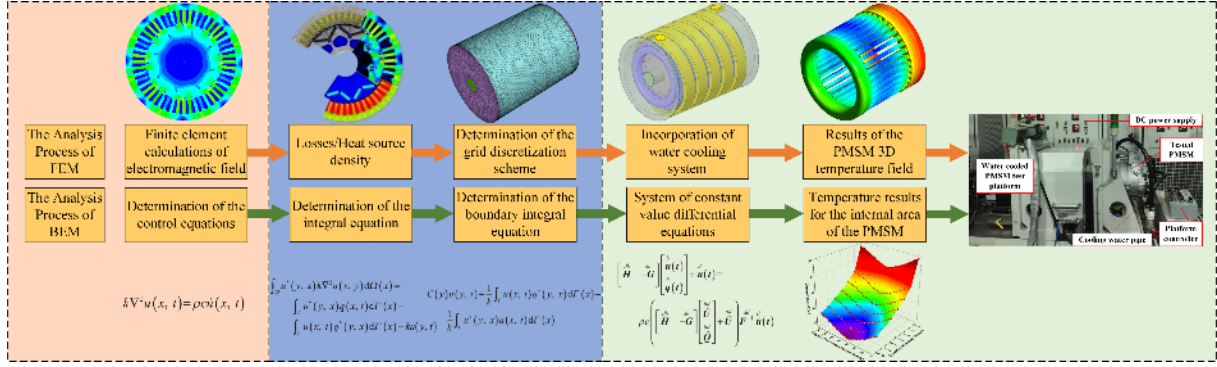


Figure 1. Calculation process for BEM, FEM

2.2. Finite element analysis

In this paper, FEM is applied to numerically calculate the temperature distribution of the PMSM for EVs. The temperature distribution of the motor at different speeds was investigated with the 3-D finite element PMSM model developed, and the heat transfer performance was tested using the made prototype. In the analysis, the 3-D finite element model was dimensioned identically to the prototype. In order to simulate the real operation of the PMSM, it is assumed that the motor is well insulated. Other assumptions are as follows:

- The fluid flow velocity inside a water-cooled system is much less than the speed of sound, so the fluid is considered incompressible.
- The turbulence model is used to solve for the flow field due to the large Reynolds number of the fluid within the water-cooled system.
- The cooling fluid is assumed to enter the inlet of the water-cooled system at a vertical angle.
- The copper loss, the stator iron loss, the rotor iron loss and the eddy current loss in the permanent magnets are evenly distributed in the windings, the stator iron core, the rotor iron core and the permanent magnets respectively during motor operation.

The heat transfer process in the PMSM is theoretically governed by the law of conservation of energy, the law of conservation of momentum and the law of conservation of mass. Of these, the law of conservation of energy is as follows:

$$\frac{\partial(\rho T)}{\partial t} + \text{div}(\rho \mathbf{u} T) = \text{div}\left(\frac{k}{c_p} \text{grad} T\right) + S_T \quad (17)$$

Where c_p is the specific heat capacity, T is the temperature of the fluid, k is the heat transfer coefficient of the fluid, and S_T is the fluid heat source.

The law of conservation of momentum is as follows:

$$\begin{aligned} \frac{\partial(\rho \mathbf{u})}{\partial t} + \text{div}(\rho \mathbf{u} \mathbf{u}) &= -\frac{\partial p}{\partial x} + \frac{\partial \tau_{xx}}{\partial x} + \frac{\partial \tau_{yx}}{\partial y} + \frac{\partial \tau_{zx}}{\partial z} + F_x \\ \frac{\partial(\rho \mathbf{v})}{\partial t} + \text{div}(\rho \mathbf{v} \mathbf{u}) &= -\frac{\partial p}{\partial y} + \frac{\partial \tau_{xy}}{\partial x} + \frac{\partial \tau_{yy}}{\partial y} + \frac{\partial \tau_{zy}}{\partial z} + F_y \\ \frac{\partial(\rho \mathbf{w})}{\partial t} + \text{div}(\rho \mathbf{w} \mathbf{u}) &= -\frac{\partial p}{\partial z} + \frac{\partial \tau_{xz}}{\partial x} + \frac{\partial \tau_{yz}}{\partial y} + \frac{\partial \tau_{zz}}{\partial z} + F_z \end{aligned} \quad (18)$$

where i is the coordinate direction, F_i is the volume force on the microelement, p is the static pressure on the fluid microelement, τ_{xx} , τ_{xy} and τ_{xz} are the viscous stress components on the surface of the microelement.

The law of conservation of mass is as follows:

$$\frac{\partial \rho}{\partial t} + \frac{\partial(\rho u)}{\partial x} + \frac{\partial(\rho v)}{\partial y} + \frac{\partial(\rho w)}{\partial z} = 0 \quad (19)$$

where ρ is the fluid density, t is the time, u , v and w is the fluid velocity.

Considering the operating conditions of the PMSM and taking into account the structural characteristics of the spiral water-cooled system, the outer wall surface of the housing is considered as the boundary condition for natural convection. The other necessary boundary conditions are as follows:

- The inlet of the water-cooled system is defined as the velocity inlet and the outlet as the pressure outlet.
- The water temperature and flow rate at the inlet of the water-cooled system are maintained at 45°C and 1.15ms⁻¹ respectively, and subsequently change as the numerical simulation proceeds.
- Based on the actual operation of the water-cooled system, the outer wall surface of the rotor is defined as a rotating wall surface with an initial speed of 4600 rpm, which is subsequently changed as the numerical simulation proceeds.

In this paper, the PMSM for EVs with the spiral water cooled system is the object of study and the specific parameters of the motor are given in Table 1.

Table 1. Detailed parameters of the prototype motor

Parameter	Value	Parameter	Value
Rated power[kW]	60	Number of stator slots	48
Rated voltage [V]	360	Number of poles	8
Rated current [A]	300	Cooling mode	water-cooled
External diameter of stator[mm]	238	Inner diameter of stator[mm]	155

To accurately calculate the steady-state temperature distribution of the PMSM at each speed range, the 3-D finite element model shown in Fig. 2 was established and solved in this investigation.

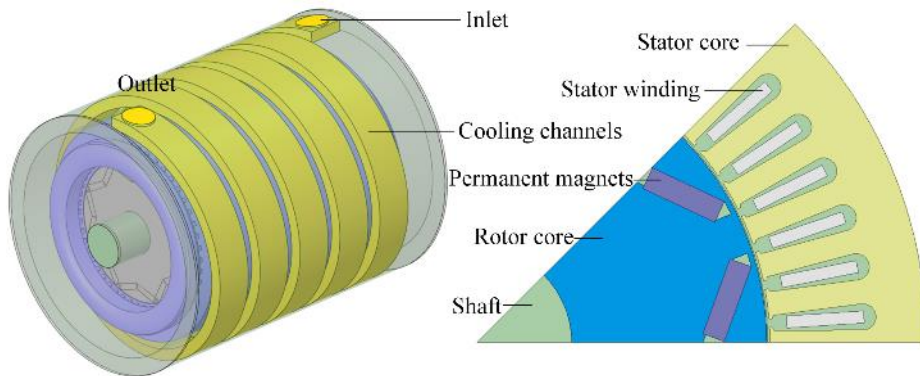


Figure 2. 3-D finite element model

Taking the maximum speed of 50 kW, 11500 rpm as an example, the magnetic flux density distribution and iron loss of the motor were calculated using the combination of Ansoft Maxwell 2D

and Ansoft Simplorer. The distribution of the magnetic flux density of the motor is shown in Fig. 3. The highest magnetic density is located at the rotor isolation bridge, with a maximum density of 1.61 T. The stator and rotor iron loss are 2.89 kW and 279 W respectively.

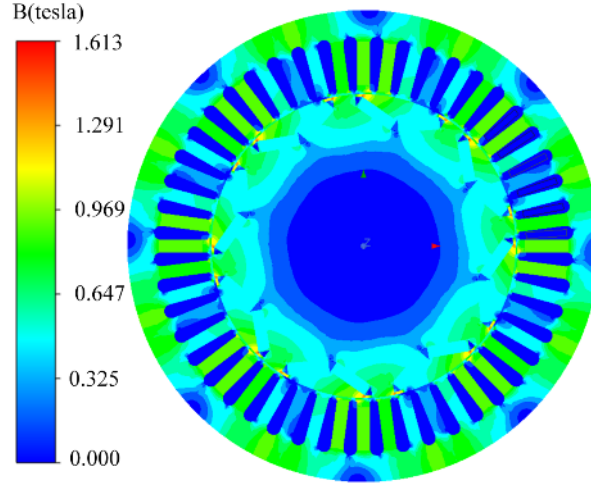


Figure 3. Magnetic flux density distribution of the PMSM

Fig. 4(a) and 4(b) show the high quality grid discretization scheme and the grid independence verification respectively. The details of the hexahedral co-nodal grid of the PMSM are shown in the enlarged view in Fig. 4(a). The overall distortion of the co-nodal grid is 0.63, thus ensuring accuracy in the calculation of the thermal behaviour of the motor. The number of grids in the 3D finite element model is 17.61 million, of which 1.52 million are used for the calculation area of the water-cooled system. The grid independence was verified by calculating the effect of different grid quantity on the turbulent kinetic energy (TKE) of the water-cooled system. When the number of grids is less than 1.52 million, the TKE decay rate of the fluid in the water-cooled system increases. However, as the number of grids increases, the rate of decay of the TKE tends to level off. 1.52 million grids compared to 1.87 million grids, the decay rate of TKE tends to be the same. Considering the accuracy and efficiency of the calculation, the final choice of grid quantity for the calculation domain of the water-cooled system is 1.52 million.

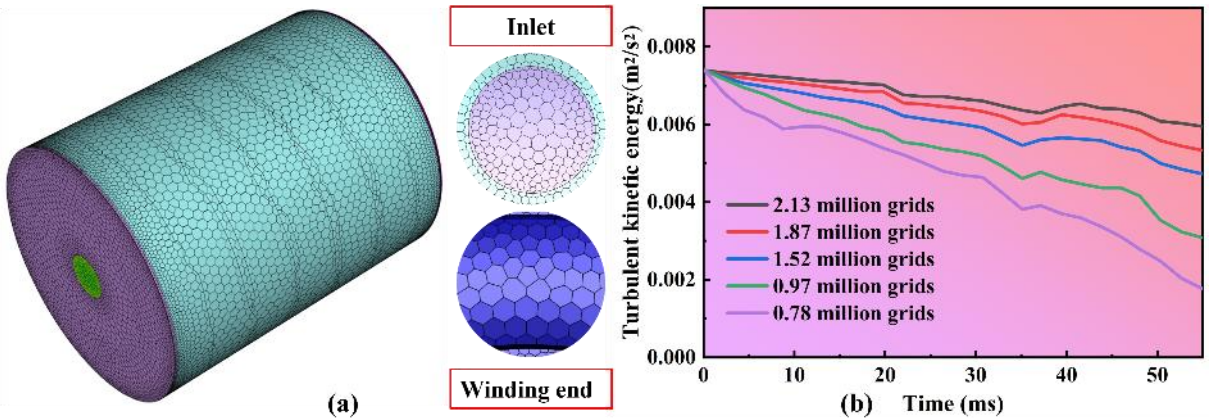


Figure 4. (a) Grid discretization scheme; (b) Grid independence verification

It is worth noting that for the BEM, with the same time step as the FEM, The number of rectangular elements in the whole calculation area is 967, the number of nodes is 7651 and the number of RBF interpolation points is 431. It can be clearly seen that both in terms of the number of elements and the number of nodes, the BEM is far less than the FEM, so the computational effort of the BEM is extremely small compared to the FEM.

3. Results and Discussion

To analyse the temperature distribution of the PMSM at different speeds, the inlet flow velocity of the water cooled system was fixed at 1.15ms^{-1} and the temperature distribution obtained for different parts of the motor is shown in Fig. 5.

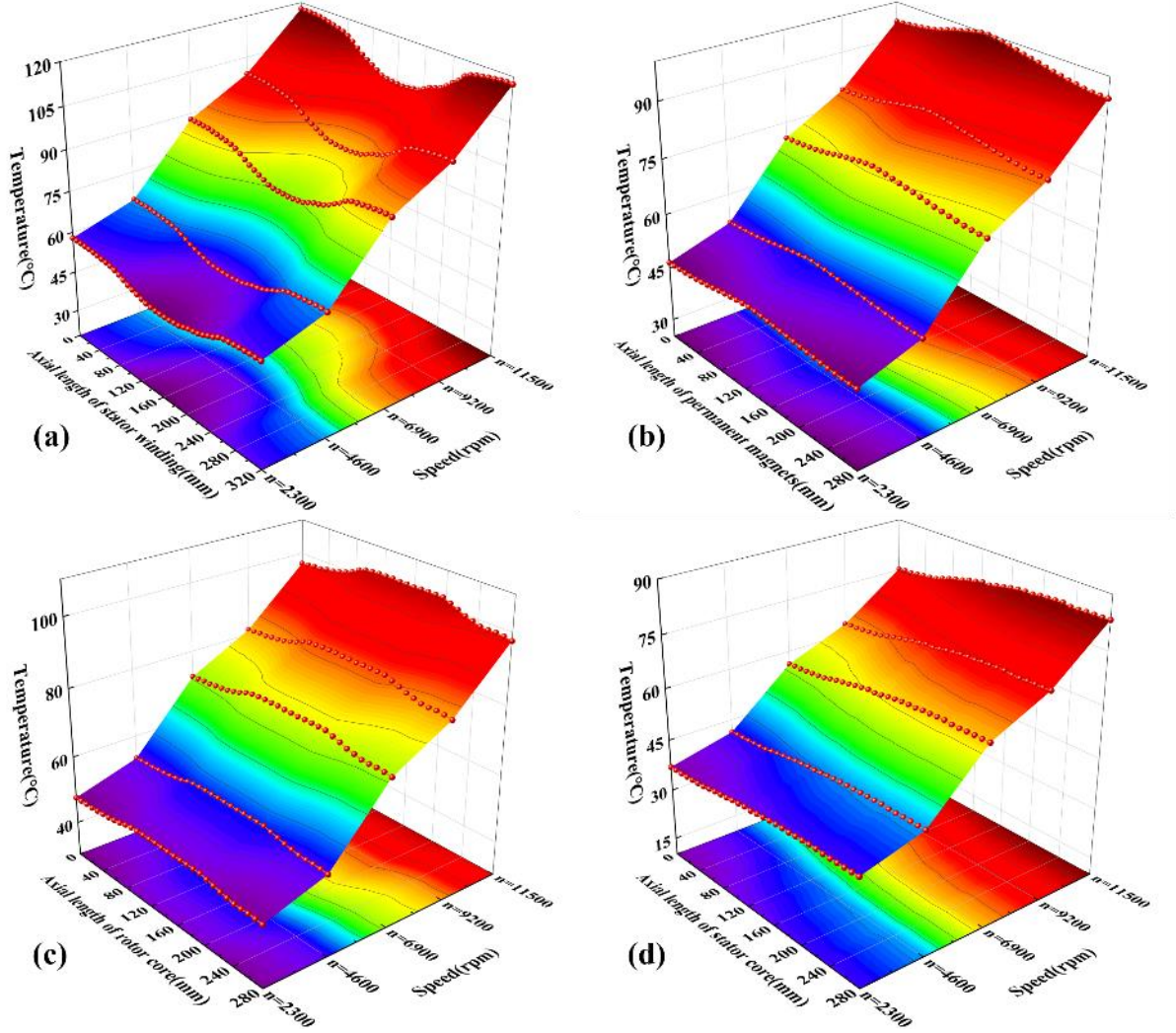


Figure 5. Finite element temperature distribution of the PMSM at different speeds (a) Stator winding. (b) Permanent magnets. (c) Rotor core. (d) Stator core.

It is clear from Fig. 5 that the temperature of each part of the motor increases as the speed increases, especially when the speed is greater than 4600 rpm, the temperature growth rate of each part increases significantly. In particular, the temperature growth rate of the stator winding and permanent magnet can reach 35.96% and 19.16% from 4600rpm to 6900rpm and 9200rpm to 11500rpm respectively. As the speed rises to 11,500 rpm, the maximum temperatures of the stator winding and permanent magnet reach 117.75°C and 94.65°C respectively.

It is worth noting that they produce their maximum temperatures in completely different locations, with the maximum temperature of the stator winding at the end and the maximum temperature of the permanent magnet at the axial centre, which is directly related to the mode of cooling of the motor. As this motor is equipped with a spiral water cooled system, the central position of the stator and rotor becomes the focus of cooling. Similarly, the cooling focus of the air-cooled system becomes the winding end area.

To ensure the accuracy of the BEM calculations, four points were selected at each major part (stator winding, permanent magnet, rotor core and stator core): A (103.24,319.41,0), B (119.67,278.13,0), C (79.81,278.13,0) and D (72.36,278.35,0). The results of the BEM calculations for points A to D at different time steps when the motor speed is at 11500 rpm are shown in Table 2.

Table 2. BEM temperature results for points A-D at different time steps

Point A					Point B				
Time [min]	$\Delta t[s]$				Time [min]	$\Delta t[s]$			
	0.1	0.5	1	2		0.1	0.5	1	2
5	117.30	118.24	118.64	119.03	5	94.20	94.78	95.17	95.49
10	117.58	118.77	119.54	120.10	10	94.43	95.21	95.89	96.35
15	117.48	118.60	119.24	119.65	15	94.35	95.07	95.64	95.98
20	117.43	118.49	118.98	119.43	20	94.31	94.98	95.44	95.81
25	117.40	118.39	118.92	119.39	25	94.29	94.90	95.39	95.78
30	117.38	118.39	118.86	119.32	30	94.27	94.90	95.34	95.72
35	117.38	118.38	118.83	119.28	35	94.27	94.89	95.32	95.69
40	117.37	118.35	118.81	119.25	40	94.26	94.87	95.30	95.66
45	117.36	118.34	118.80	119.24	45	94.25	94.86	95.29	95.65
50	117.34	118.33	118.78	119.21	50	94.24	94.85	95.27	95.64
Point C					Point D				
Time [min]	$\Delta t[s]$				Time [min]	$\Delta t[s]$			
	0.1	0.5	1	2		0.1	0.5	1	2
5	96.64	97.43	97.87	98.03	5	75.83	76.67	77.18	77.32
10	96.93	97.96	98.45	98.93	10	76.13	77.23	77.94	78.10
15	96.80	97.70	98.33	98.71	15	76.04	76.96	77.60	77.92
20	96.75	97.67	98.18	98.58	20	75.95	76.88	77.52	77.78
25	96.74	97.61	98.11	98.49	25	75.93	76.83	77.48	77.66
30	96.73	97.58	98.07	98.42	30	75.91	76.81	77.42	77.62
35	96.72	97.56	98.03	98.35	35	75.91	76.80	77.40	77.60
40	96.71	97.55	98.01	98.30	40	75.89	76.78	77.38	77.56
45	96.70	97.52	97.99	98.29	45	75.88	76.77	77.35	77.53
50	96.70	97.52	97.97	98.29	50	75.88	76.76	77.34	77.52

From Table 2 it can be concluded that, at the four different time steps given, the maximum difference in temperature obtained by BEM compared to FEM for the stator windings and permanent magnets is 2.35°C and 1.70°C respectively, occurring around the 10th min moment at a time step of 2 s. To further analyse the difference in temperature calculation between the BEM and FEM during PMSM operation and to verify the accuracy and validity of the BEM calculation results, the following relative errors are defined:

$$e_{\text{ror}} = \frac{\sqrt{\sum_{i=1}^N (T_i^{\text{FEM}} - T_i^{\text{BEM}})^2}}{N} \frac{1}{\max_j |T_i^{\text{BEM}}|} \quad (20)$$

where M is the subdivision parameter and P is the truncation parameter.

Considering the relative errors of the BEM results and the FEM results at different time steps, the resulting results are shown in Fig. 6.

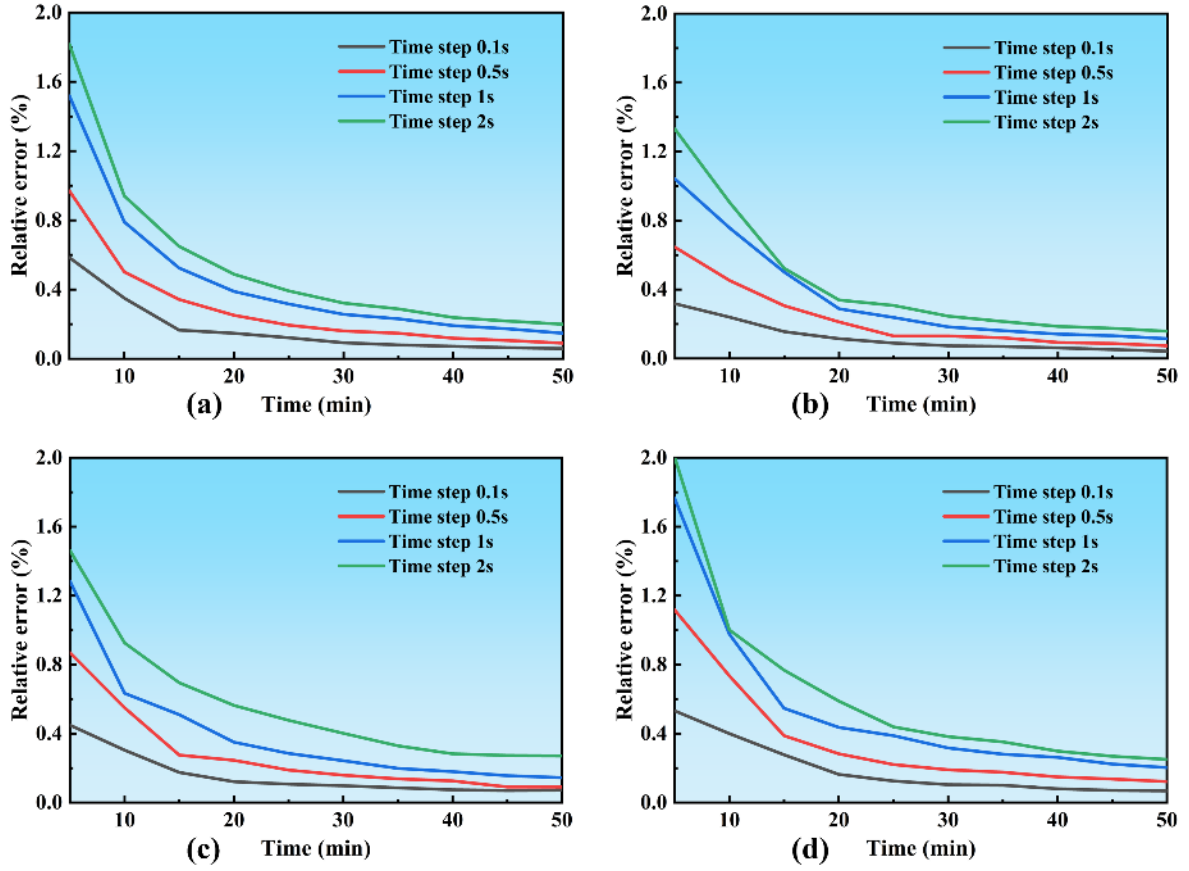


Figure 6. Relative error curve of temperature over time (a) Stator winding. (b) Permanent magnets. (c) Rotor core. (d) Stator core.

Fig. 6 illustrates the relative error curves of the temperature calculations of the FEM and BEM with time for the PMSM at four different time steps. When the time step is 0.1s, the relative error curve is located at the bottom of each figure, indicating that it has the smallest relative error at the same moment in time. Even at the initial moments, a certain relative error does exist between the temperature calculation results of the FEM and the BEM, with the largest relative error occurring during the calculation of the stator core, where the maximum relative error is 1.97%. However, as time progresses, the FEM and BEM calculation results for all time steps are in increasingly high agreement.

4. Experimental verification

To verify the accuracy of the BEM numerical calculations and FEM simulation calculations, an EV PMSM with a rated power of 60kW was made and equipped with a spiral water cooled system for the motor. The built motor temperature test platform is shown in Fig. 7(a) and a comparison of the calculated and test results is shown in Fig. 7(b). To measure the stator winding temperature, thermocouples were placed on the inside of the motor end windings to measure the temperature.

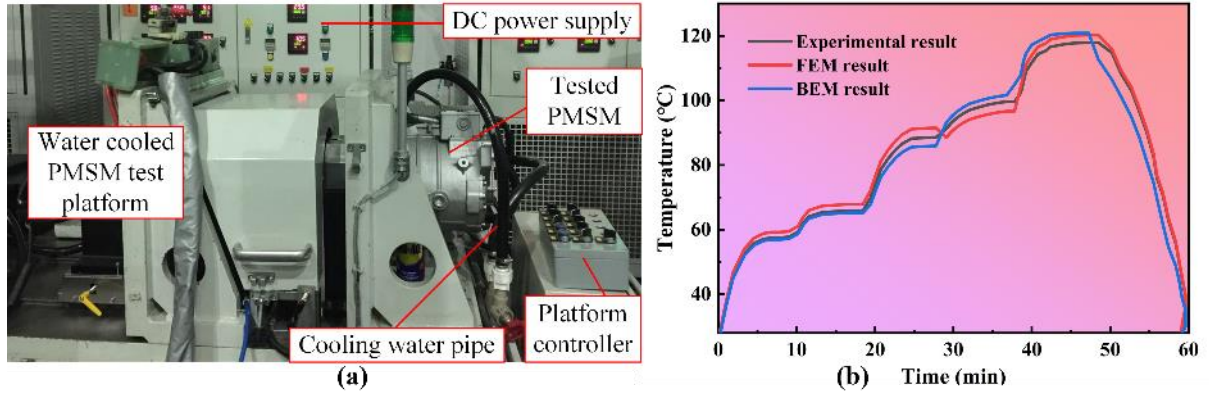


Figure 7. (a)Test platform (b) Comparison of FEM, BEM and test results

To ensure the accuracy of the test, the motor was ramped up to 2300rpm, 4600rpm, 6900rpm, 9200rpm and 11500rpm throughout the test, with a running time of 10 minutes for each speed. Although there was a relative error between the numerical calculations and the test results of less than 3% around the 30th minute. However, in general, the results of the two numerical calculation methods still fit well with the test results and the maximum relative error meets the actual engineering requirements. The reason for the relative error is that, in the BEM calculation process, the RBF is used to interpolate the unknown quantities to approximate them. During the FEM simulation, the automatic repair of the residual factor leads to a slight distortion in the temperature growth rate in some speed intervals.

5. Conclusion

For the steady-state heat transfer problem of PMSM for EVs, this work uses BEM and FEM to comparatively investigate it and conducts secondary experimental comparisons under multi-speed conditions, the results obtained verified the validity and accuracy of BEM in calculating the heat transfer problem of water-cooled PMSM, and summarises the following main findings.

- (1) For the field of PMSM heat transfer, the BEM is used for the first time to calculate the steady-state temperature distribution of the motor. The BIE applicable to the steady-state heat transfer problem of water-cooled PMSM is derived, a system of constant coefficient differential equations is obtained by discretizing the boundaries, and the temperature results obtained are compared with the simulation results of the FEM.
- (2) There is a relative error between the temperature calculation results of the FEM and the BEM, with the largest relative error occurring at the initial moment of the stator core calculation, with a maximum relative error of 1.97%. the RBF selection of the BEM and the residual factor of the FEM are the two main causes of the relative error.
- (3) Although the relative error in the numerical calculations compared to the test results is less than 3% in the speed range of 6900rpm to 9200rpm. However, the numerical calculation results of BEM and FEM are still in high agreement with the test results. This proves that the BEM has the same reliability and accuracy as the FEM, and that the BEM has the advantages of small calculation volume and high calculation accuracy.

The research in this paper is limited and the following research can be carried out on this basis in the future: the PMSM investigated in this paper is matched with a spiral water cooled system, for

which a PMSM with an axial water cooled system or a circumferential water cooled system could be the subject of future BEM research.

References

- [1] I. Petrov., *et al.*, Investigation of a Direct Liquid Cooling System in a Permanent Magnet Synchronous Machine. *IEEE Transactions on Energy Conversion*, 35 (2020), 2, pp. 808-817
- [2] D. Speth., *et al.*, Comparing Options to Electrify Heavy-duty Vehicles: Findings of German Pilot Projects. *World Electric Vehicle Journal*, 12 (2021), pp. 67-74
- [3] G. Du., *et al.*, Power Loss and Thermal Analysis for High-Power High-Speed Permanent Magnet Machines. *IEEE Transactions on Industrial Electronics*, 67 (2020), 4, pp. 2722-2733
- [4] L. Xu., *et al.*, Comparative Analysis and Design of Partitioned Stator Hybrid Excitation Axial Flux Switching PM Motors for in-Wheel Traction Applications. *IEEE Transactions on Energy Conversion*, 37 (2022), 2, pp. 1416-1427
- [5] M. Kang., *et al.*, Self-circulation Cooling Structure Design of Permanent Magnet Machines for Electric Vehicle. *Applied thermal engineering*, 165 (2020), pp. 114593
- [6] Y. Gai., *et al.*, Numerical and Experimental Calculation of CHTC in an Oil-based Shaft Cooling System for a High-speed High-power PMSM. *IEEE Transactions on Industrial Electronics*, 67 (2020), 6, pp. 4371-4380
- [7] Zhang, Y., *et al.*, A Space-Vector-Modulation-Based Thermal Calculation Method for Surface-Mounted Permanent Magnet Synchronous Motor. *IEEE Transactions on Magnetics*, 56 (2020), 6, pp. 1-9
- [8] V. Madonna., *et al.*, Thermal Overload and Insulation Aging of Short Duty Cycle, Aerospace Motors. *IEEE Transactions on Industrial Electronics*, 67 (2020), 4, pp. 2618-2629
- [9] J.W. Chin., *et al.*, High Efficiency PMSM with High Slot Fill Factor Coil for Heavy-duty EV Traction Considering AC Resistance. *IEEE Transactions on Energy Conversion*, 36 (2020), 2, pp. 883-894
- [10] Li, S., *et al.*, Improvement of The Thermal Field of PMSM with Optimized Groove Structure. *Journal of Thermal Science and Engineering Applications*, 13 (2021), 1, pp. 011010
- [11] A. Tessarolo., *et al.*, Fast Computation Method for Stator Winding Skin-Effect Additional Losses in Synchronous Machines with Open Slots and Arbitrary Rotor Geometry. *IEEE Transactions on Energy Conversion*, 36 (2020), 2, pp. 1156-1168
- [12] Wu, R., *et al.*, A Comparative Study of Heat Transfer Characteristics between PMSM and IPMSM and Thermal Optimization of PMSM based on Fluid Structure Coupling. *IEEE Transactions on Industrial Electronics*, 68(2020), 11, pp. 10483-10494
- [13] J. Chang., *et al.*, A Yokeless and Segmented Armature Axial Flux Machine with Novel Cooling System for In-Wheel Traction Applications. *IEEE Transactions on Industrial Electronics*, 68 (2021), 5, pp. 4131-4140
- [14] W. Li., *et al.*, Thermal Analysis of the Solid-Rotor Permanent Magnet Synchronous Motors with Air-cooled Hybrid Ventilation Systems. *IEEE Transactions on Industrial Electronics*, 69 (2021), 2, pp. 1146-1156
- [15] H. Vansompel., *et al.*, Extended End-Winding Cooling Insert for High Power Density Electric Machines with Concentrated Windings. *IEEE Transactions on Energy Conversion*, 35 (2020), 2, pp. 948-955

- [16] Xu, X., *et al.*, Thermal Modeling and Testing of A Flux-Switching Permanent Magnet PMSM with Air Impingement Cooling. *IEEE Transactions on Industry Applications*, 56, (2019), 3, pp. 2747-2759
- [17] Rashed S., *et al.*, A Boundary Element Method for Accurate Thermal Analysis of Power Transformers. *Energy Conversion and Management*, 206, (2020), pp. 12-18
- [18] Bonari J., *et al.*, A Multi-scale FEM-BEM Formulation for Contact Mechanics between Rough Surfaces. *Computational Mechanics*, 65 (2020), pp. 731-749
- [19] Neto A R., *et al.*, One Step forward towards the Full Integration of BEM and CAD Software: An Effective Adaptive Approach. *Engineering Analysis with Boundary Elements*, 143 (2022), pp. 457-482
- [20] Qin F., *et al.*, The Application of FEM-BEM Coupling Method for Steady 2D Heat Transfer Problems with Multi-scale Structure. *Engineering Analysis with Boundary Elements*, 137 (2022), pp. 78-79
- [21] Gong Y., *et al.*, An Isogeometric Boundary Element Method for Heat Transfer Problems of Multiscale Structures in Electronic Packaging with Arbitrary Heat Sources. *Applied Mathematical Modelling*, 109 (2022), pp. 161-185
- [22] Si Y., *et al.*, Prediction and Evaluation of Energy and Exergy Efficiencies of A Nanofluid-Based Photovoltaic-thermal System with A Needle Finned Serpentine Channel Using Random Forest Machine Learning Approach. *Engineering Analysis with Boundary Elements*, 151 (2023), pp. 328-343
- [23] Zhu C., *et al.*, Numerical Simulation and Optimization with Artificial Neural Network of Two-phase Nanofluid Flow in A Circular Heatsink with Cylindrical Pin-fins. *Engineering Analysis with Boundary Elements*, 148 (2023), pp. 305-316
- [24] F.L. Zhou., *et al.*, Transient heat conduction analysis of heat dissipation structure based on time domain boundary element method. *Journal of Hunan University of Technology*, 36 (2022), 3, pp. 222-28

Submitted: 22.05.2023.

Revised: 21.06.2023.

Accepted: 22.06.2023.